Floquet approach to $\mathbb{Z}_2$ lattice gauge theories with ultracold atoms in optical lattices

Christian Schweizer[1,2,3], Fabian Grusdt [ID][3,4], Moritz Berngruber[1,3], Luca Barbiero[5], Eugene Demler[6], Nathan Goldman[5], Immanuel Bloch[1,2,3] and Monika Aidelsburger [ID][1,2,3]*

Quantum simulation has the potential to investigate gauge theories in strongly interacting regimes, which are currently inaccessible through conventional numerical techniques. Here, we take a first step in this direction by implementing a Floquet-based method for studying $\mathbb{Z}_2$ lattice gauge theories using two-component ultracold atoms in a double-well potential. For resonant periodic driving at the on-site interaction strength and an appropriate choice of the modulation parameters, the effective Floquet Hamiltonian exhibits $\mathbb{Z}_2$ symmetry. We study the dynamics of the system for different initial states and critically contrast the observed evolution with a theoretical analysis of the full time-dependent Hamiltonian of the periodically driven lattice model. We reveal challenges that arise due to symmetry-breaking terms and outline potential pathways to overcome these limitations. Our results provide important insights for future studies of lattice gauge theories based on Floquet techniques.

attice gauge theories (LGTs)[1,2] are fundamental for our understanding of quantum many-body physics across different disciplines ranging from condensed matter[3–6] to high-energy physics[7]. However, theoretical studies of LGTs can be extremely challenging—particularly in strongly interacting regimes, where conventional computational methods are limited[8,9]. To overcome these limitations, alternative numerical tools have been developed, which enable out-of-equilibrium and finite-density computations[10–13]. In parallel, the rapid progress in the field of quantum simulation[14–17] has sparked a growing interest in designing experimental platforms to explore the rich physics of LGTs[18–25]. State-of-the-art experiments are now able to explore the physics of static[26] as well as density-dependent gauge fields[27] and have engineered controlled few-body interactions[28–30], which are the basis for many proposed schemes to realize LGTs. First studies of the Schwinger model have been performed with quantum-classical algorithms[31] and a digital quantum computer composed of four trapped ions[32]. The challenge for analogue quantum simulators mainly lies in the complexity to engineer gauge-invariant interactions between matter and gauge fields.

Here, we explore the dynamics of a minimal model for $\mathbb{Z}_2$ LGTs coupled to matter with ultracold atoms in periodically driven double-well potentials[33]. An alternative technique was recently proposed for digital quantum simulation[34]. $\mathbb{Z}_2$ LGTs are of high interest in condensed matter physics[13,35–37] and topological quantum computation[38]. Our scheme is based on density-dependent laser-assisted tunnelling techniques[39–42]. We use a mixture of bosonic atoms in two different internal states to encode the matter and gauge field degrees of freedom. The interaction between these states is engineered via resonant periodic modulation[43–46] of the on-site potential at the inter-species Hubbard interaction[47–50]. By choosing suitable modulation parameters, the effective Floquet model exhibits a $\mathbb{Z}_2$ symmetry[33]. We present a detailed study of this effective Floquet model defined on a double well, which constitutes the basic building block of the LGT. We discuss the relation between the observed

dynamics and the ideal model and reveal the potential impact of symmetry-breaking terms.

To understand the observed phenomena, it is instructive to consider the properties of an extended one-dimensional (1D) $\mathbb{Z}_2$ LGT, as captured by the Hamiltonian

$$\hat{H}_{\mathbb{Z}_2} = -\sum_j J_a \left(\hat{\tau}^z_{\langle j,j+1 \rangle} \hat{a}^\dagger_j \hat{a}_{j+1} + \text{h.c.} \right) - \sum_j J_f \hat{\tau}^x_{\langle j,j+1 \rangle} \quad (1)$$

Here $\hat{a}^\dagger_j$ describes the creation of a matter particle on lattice site j and the Pauli operators $\hat{\tau}_{\langle j,j+1 \rangle}$, defined on the links between neighbouring lattice sites, encode the gauge field degrees of freedom. The elementary ingredients of this $\mathbb{Z}_2$ LGT are illustrated in Fig. 1a. Note that the illustrations of the $\mathbb{Z}_2$ gauge field and $\mathbb{Z}_2$ electric field are related to the physical implementation of the building block, which is discussed later in the text. The matter field has a charge $\hat{Q}_j = e^{i\pi \hat{n}^a_j}$ on site j, which is given by the parity of the site occupation, with $\hat{n}^a_j = \hat{a}^\dagger_j \hat{a}$ the number operator. The dynamics of the matter field is coupled to the $\mathbb{Z}_2$ gauge field $\hat{\tau}^z_{\langle j,j+1 \rangle}$ with an amplitude J_a. The energy scale associated with the electric field $\hat{\tau}^x_{\langle j,j+1 \rangle}$ is J_f.

The model Hamiltonian (equation (1)) commutes with the lattice gauge transformations defined by the local symmetry operators

$$\hat{G}_j = \hat{Q}_j \prod_{i:\langle i,j \rangle} \hat{\tau}^x_{\langle i,j \rangle}, \qquad [\hat{H}, \hat{G}_j] = 0 \quad \forall j \quad (2)$$

where $\prod_{i:\langle i,j \rangle}$ denotes the product over all nearest-neighbour links connected to lattice site j. The eigenvalues of $\hat{G}_j$ are $g_j = \pm 1$. The dynamics of the model is constrained by $\mathbb{Z}_2$ Gauss's law, $\hat{G}_j |\psi\rangle = g_j |\psi\rangle$, in analogy to electrodynamics. Since the local values g_j are conserved, the motion of $\mathbb{Z}_2$ charges is coupled to a change of the $\mathbb{Z}_2$ electric field lines on the link connecting the two lattice sites. Gauss's law effectively separates the Hilbert space into different subsectors, which are characterized by a set of conserved quantities $\{g_j\}$.
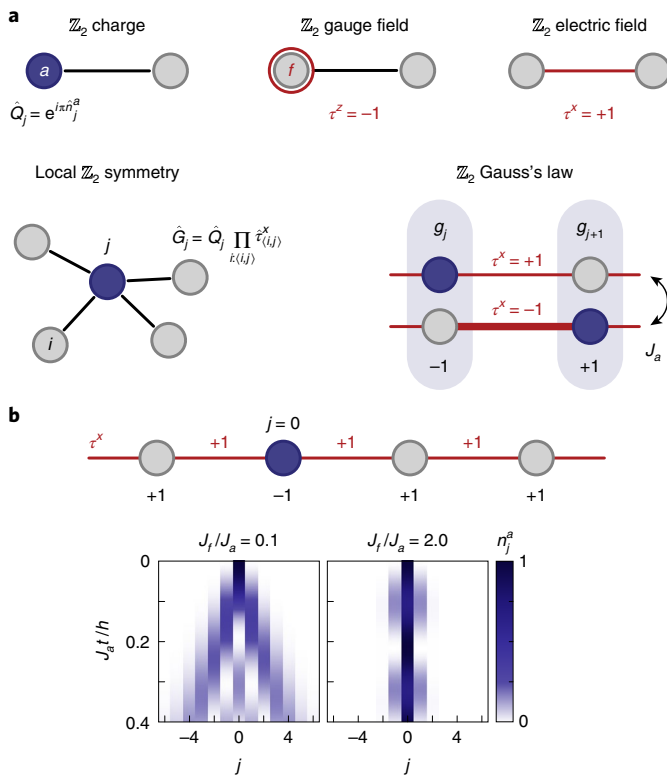
Fig. 1 | 1D $\mathbb{Z}_2$ lattice gauge theory coupled to matter. Circles indicate lattice sites, which are empty (grey) or occupied by a matter particle (blue). Red circles and the thickness of red links illustrate the expectation value of the link operators, τ^z and τ^x. **a**, Elementary ingredients: $\mathbb{Z}_2$ charge $\hat{Q}_j = e^{i\pi\hat{n}_j^a}$, $\mathbb{Z}_2$ gauge field $\hat{\tau}_{\langle j,j+1\rangle}^z$, $\mathbb{Z}_2$ electric field $\hat{\tau}_{\langle j,j+1\rangle}^x$, and local symmetry operator $\hat{G}_j$ with conserved quantities g_j. Here $i:\langle i,j\rangle$ denotes all lattice sites i connected to site j via a nearest-neighbour link, denoted as $\langle i,j\rangle$. Matter and gauge fields are implemented using two different species, denoted as a (blue) and f (red). Matter–gauge coupling occurs with strength J_a. **b**, Dynamics of the 1D model (equation (1)) for different values of J_f/J_a calculated with exact diagonalization of a system with 13 sites based on equation (1). The initial state is a single matter particle located on site $j=0$ and the gauge field is in an eigenstate of the electric field.

The two configurations sketched in Fig. 1a (lower right) belong to the same subsector and illustrate the basic matter–gauge coupling according to Gauss's law. Lattice sites with $g_j = -1$ are interpreted as local static background charges (Supplementary Information). Different subsectors can be explored by preparing suitable initial states.

To gain more insight into the physics of the 1D model (equation (1)), we consider a system initially prepared in an eigenstate of the electric field operator, with $\tau^x = +1$ on all links, and a single matter particle located on site $j=0$. For this initial state $g_j = +1$, $\forall j \neq 0$ and $g_j = -1$ for $j=0$ (Fig. 1b). In the limit of vanishing electric field energy $J_f \to 0$, the matter particle can tunnel freely along the 1D chain, thereby changing the electric field on all traversed links. For $J_f \neq 0$, tunnelling of the matter particle is detuned due to the energy of the electric field and the matter particle is bound to the location of the static background charge at $j=0$. In this regime, the energy of the system scales linearly with the distance between the static charge and the matter particle, which we interpret as a signature of confinement (Supplementary Information).

Here, we engineer the elementary interactions of the $\mathbb{Z}_2$ model on a two-site lattice following ref. [33]. The matter and gauge fields

are implemented using two different species denoted a and f particles, which are realized by two Zeeman levels of the hyperfine ground-state manifold of ^{87}Rb, $|a\rangle \equiv |F=1, m_F = -1\rangle$ and $|f\rangle \equiv |F=1, m_F = +1\rangle$. We prepare one a and one f particle in each two-site system. The matter field is associated with the a particle. The $\mathbb{Z}_2$ gauge field is the number imbalance $\hat{\tau}_{\langle j,j+1\rangle}^z = \hat{n}_{j+1}^f - \hat{n}_j^f$ of the f particle and the $\mathbb{Z}_2$ electric field corresponds to tunnelling of the f particle, $\hat{\tau}_{\langle j,j+1\rangle}^x = \hat{f}_j^\dagger \hat{f}_{j+1} + \hat{f}_{j+1}^\dagger \hat{f}_j$, where $\hat{f}_j^\dagger$ is the creation operator of an f particle on site j and $\hat{n}_j^f = \hat{f}_j^\dagger \hat{f}_j$ is the corresponding number-occupation operator. An extension of our scheme to realize extended 1D LTGs is presented in the Supplementary Information. It requires exactly one f particle per link, while the density of a particles (fermions or hard-core bosons) can take arbitrary values.

The driving scheme is based on a species-dependent double-well potential with tunnel coupling J between neighbouring sites and an energy offset Δ_f only seen by the f particle. Experimentally, it is realized with a magnetic-field gradient, making use of the opposite magnetic moments of the two states $|a\rangle$ and $|f\rangle$ (Supplementary Information). In the limit of strong on-site interactions $U \gg J$ (where U is the on-site Hubbard interaction), first-order tunnelling processes are suppressed but can be restored resonantly with a periodic modulation at the resonance frequency $\hbar\omega = \sqrt{U^2 + 4J^2} \approx U$. The full time-dependent Hamiltonian can be expressed as

$$\hat{H}(t) = -J\left(\hat{a}_2^\dagger \hat{a}_1^\dagger + \hat{f}_2^\dagger \hat{f}_1^\dagger + \text{h.c.}\right)$$
$$+ U \sum_{j=1,2} \hat{n}_j^a \hat{n}_j^f + \Delta_f \hat{n}_1^f \qquad (3)$$
$$+ A\cos(\omega t + \phi)\left(\hat{n}_1^a + \hat{n}_1^f\right)$$

where A is the modulation amplitude and ϕ is the modulation phase. For resonant modulation $\hbar\omega \approx U$ and in the high-frequency limit $\hbar\omega \gg J$, the lowest order of the effective Floquet Hamiltonian contains renormalized tunnelling matrix elements for both a and f particles[44–46]. For general modulation parameters, the amplitudes and phases are operator-valued and explicitly depend on the site-occupations. For certain values of the modulation phase ($\phi = 0$ or π), however, these expressions simplify and realize the $\mathbb{Z}_2$ model. The driving scheme can be understood by considering the individual photon-assisted tunnelling processes of a and f particles in situations, where one of the two particles is localized on a particular site of the double well. This generates an occupation-dependent energy offset for the other particle, which is equal to U (Fig. 2a). For all configurations, tunnelling is resonantly restored for energy differences $\nu\hbar\omega$ between neighbouring sites with renormalized tunnelling $J\mathcal{J}_\nu(\chi)e^{i\nu\phi}$; here ν is an integer, $\mathcal{J}_\nu$ is the νth-order Bessel function of the first kind and $\chi = A/(\hbar\omega)$ the dimensionless driving parameter.

For $\phi = 0$, we find that the strength of a particle tunnelling is density-independent $J_a = J|\mathcal{J}_{\pm 1}(\chi)|$, however, depending on the position of the f particle, the on-site energy difference between neighbouring sites is either $+U$ or $-U$ (Fig. 2a). This results in a sign-dependence of the renormalized tunnelling $\pm J_a$, which stems from the property of odd Bessel functions $\mathcal{J}_{-\nu}(\chi) = (-1)^\nu \mathcal{J}_\nu(\chi)$ (Supplementary Information) and is central to our implementation of the $\mathbb{Z}_2$ symmetry[33]. It allows us to write the renormalized hopping of a particles as $J_a \hat{\tau}_{\langle 1,2\rangle}^z$. Note that we drop the link index from now on to simplify notations, $\hat{\tau} \equiv \hat{\tau}_{\langle 1,2\rangle}$.

Tunnelling of f particles becomes real-valued, with an amplitude that only weakly depends on the position of the a particle. Due to the species-dependent tilt $\Delta_f = U$, the on-site energy difference between neighbouring sites is either $\Delta_f - U = 0$ or $\Delta_f + U = 2U$ (Fig. 2a). Therefore, tunnelling is renormalized via zero- and two-photon processes, resulting in the real-valued tunnelling matrix
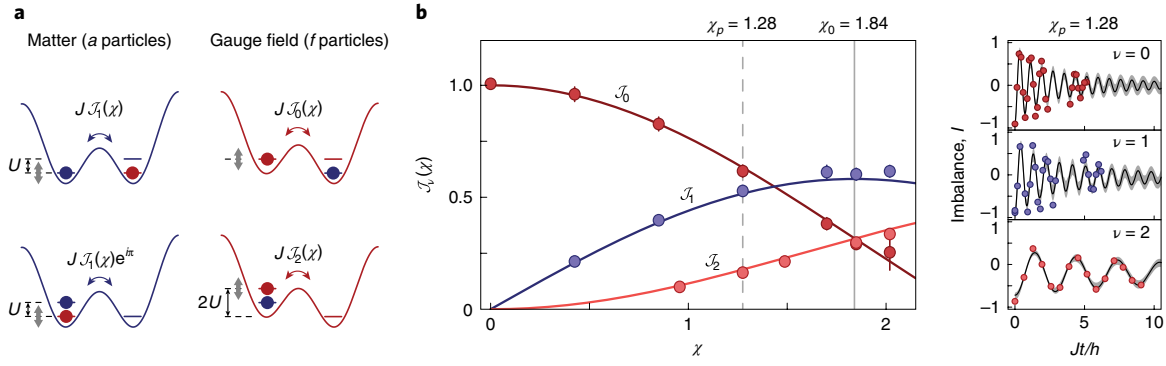
Fig. 2 | Driving scheme for $\mathbb{Z}_2$ LGTs on a double well. a, Effective tunnelling processes for the matter-field (blue, a) and gauge-field (red, f) particle. For $\phi = 0$, hopping of a particles occurs for resonant one-photon processes at $\hbar\omega \approx U$ with an effective amplitude $J\mathcal{J}_1(\chi)$, where U is the interspecies on-site interaction. Depending on the position of the f particle, the a particle acquires a phase shift of π, which realizes the matter–gauge coupling. Tunnelling of the f particle is renormalized by zero- or induced via two-photon processes, with amplitudes $J\mathcal{J}_0(\chi)$ and $J\mathcal{J}_2(\chi)$ depending on the a particle's position. **b**, Experimental results for the renormalization of the tunnel couplings $\mathcal{J}_\nu(\chi)$ for single-particle ν-photon processes $\nu = \{0, 1, 2\}$, with $\omega = 2\pi \times 4{,}122\,\text{Hz}$ and $J/h \approx 0.5\,\text{kHz}$. The solid lines are the Bessel functions, where χ was calibrated by fitting the zeroth-order Bessel function to the dark red data points (Supplementary Information). The time traces of the imbalance I are fitted with sinusoidal functions taking into account an inhomogeneous tilt distribution (solid black line) and shown for exemplary traces at $\chi_p = 1.28$ (dashed vertical line, left panel) on the right. The solid grey vertical line marks the value χ_0, where $\mathcal{J}_0(\chi_0) = \mathcal{J}_2(\chi_0)$. The error bars and the grey shading are the 1σ confidence interval obtained from a bootstrap analysis of 1,000 repetitions (Supplementary Information).

elements $J\mathcal{J}_0(\chi)$ and $J\mathcal{J}_2(\chi)$. To lowest order, the effective double-well Hamiltonian takes the form

$$\hat{H}_{\text{eff}} = -J_a \hat{\tau}^z \left(\hat{a}_2^\dagger \hat{a}_1 + \hat{a}_1^\dagger \hat{a}_2 \right) - \hat{J}_f \hat{\tau}^x \qquad (4)$$

where $\hat{J}_f$ depends on the position of the a particle

$$\hat{J}_f = J\mathcal{J}_0(\chi)\hat{n}_1^a + J\mathcal{J}_2(\chi)\hat{n}_2^a \qquad (5)$$

The density dependence of $\hat{J}_f$ can be avoided by choosing the dimensionless driving strength χ such that $\mathcal{J}_0(\chi_0) = \mathcal{J}_2(\chi_0)$, which occurs, for example, at $\chi_0 \approx 1.84$. Then, equation (4) reduces to the two-site version of the $\mathbb{Z}_2$ LGT described by Hamiltonian (equation (1)). Note that the double-well model defined in equation (4) is $\mathbb{Z}_2$-symmetric for all values of the driving strength χ.

The experimental set-up consists of a 3D optical lattice generated at wavelength $\lambda_s = 767\,\text{nm}$. Along the x axis an additional standing wave with wavelength $2\lambda_s = 1{,}534\,\text{nm}$ is superimposed to create a superlattice potential. For deep transverse lattices and suitable superlattice parameters, an array of isolated double-well potentials is realized, where all dynamics is restricted to the two double-well sites (Supplementary Information). The periodic drive is generated by modulating the amplitude of an additional lattice with wavelength $2\lambda_s$, whose potential maxima are aligned relative to the double-well potential to modulate only one of the two sites. This enables the control of the modulation phase, which is set to $\phi = 0$ or π.

We first study the renormalization of the tunnelling matrix elements for the relevant ν-photon processes[49,51–54] with a single atom on each double well (Fig. 2b). For every measurement, the atom is initially localized on the lower-energy site with a potential energy difference $\Delta_\nu \approx \nu\hbar\omega$ to the higher-energy site, where $\nu \in \{0, 1, 2\}$. Then, the resonant modulation is switched on rapidly at frequency ω and we evaluate the imbalance $I = n_2 - n_1$ as a function of the evolution time, where n_j is the density on site j. These densities were determined using site-resolved detection methods[29]. Note, this technique provides an average of this observable over the entire 3D array of double-well potentials. Hence, an overall harmonic confinement and imperfect alignment of the lattice laser beams introduces an

inhomogeneous tilt distribution $\Delta(x, y, z)$, which leads to dephasing of the averaged dynamics. The renormalized tunnelling amplitude is obtained from the oscillation frequency of the imbalance and by numerically taking into account the tilt distribution $\Delta(x, y, z)$ (Fig. 2b). We find that our data agree well with the expected Bessel-type behaviour for the ν-photon processes (Supplementary Information). Moreover, these measurements enable us to directly determine the value of the modulation amplitude, for which $\mathcal{J}_0(\chi_0) = \mathcal{J}_2(\chi_0)$, as indicated by the vertical line in Fig. 2b.

To study the dynamics of the $\mathbb{Z}_2$ double-well model (equation (4)), we prepare two different kinds of initial states, where the gauge field particle is either prepared in an eigenstate of the electric field $\hat{\tau}^x$ (Fig. 3) or the gauge field operator $\hat{\tau}^z$ (Fig. 4a). In both cases the matter particle is initially localized on site $j = 1$.

First, we consider the state $\left| \psi_0^x \right\rangle = \left| a, 0 \right\rangle \otimes (\left| f, 0 \right\rangle + \left| 0, f \right\rangle)/\sqrt{2}$ (Fig. 3a), where the gauge-field particle is in a symmetric superposition between the two sites. This state is an eigenstate of $\hat{G}_j$ defined in equation (2). The corresponding eigenvalues are $g_1 = -1$ and $g_2 = +1$. After initiating the dynamics by suddenly turning on the resonant modulation, we expect that the matter particle starts to tunnel to the neighbouring site ($j = 2$) according to the matter–gauge coupling. Depending on the energy of the electric field J_f, this process can be energetically detuned and the matter particle does not fully tunnel to the other site. Solving the dynamics according to Hamiltonian (equation (4)) analytically, gives:

$$\left\langle \hat{Q}_1(t) \right\rangle = -\frac{J_f^2 + J_a^2 \cos\left(2t\sqrt{J_f^2 + J_a^2}\right)}{J_f^2 + J_a^2} \qquad (6)$$

The maximum value of $\langle \hat{Q}_1 \rangle$ is limited to $(J_a^2 - J_f^2)/(J_a^2 + J_f^2)$. The experimental configuration is well suited to explore the regime $J_f/J_a = \mathcal{J}_0(\chi_0)/\mathcal{J}_1(\chi_0) \approx 0.54$, which corresponds to an intermediate regime between the two limiting cases discussed in Fig. 1c. These cases can also be understood at the level of the two-site model. In the weak electric field regime ($J_f/J_a \ll 1$) the matter particle tunnels freely between the two sites, while in the limit of a strong electric field ($J_f/J_a \gg 1$) the matter particle remains localized.

In the experiment we can directly access the value of the charge operator $\hat{Q}_j = e^{i\pi\hat{n}_j^a}$ and the link operator $\hat{\tau}^z = \hat{n}_2^f - \hat{n}_1^f$ via site- and
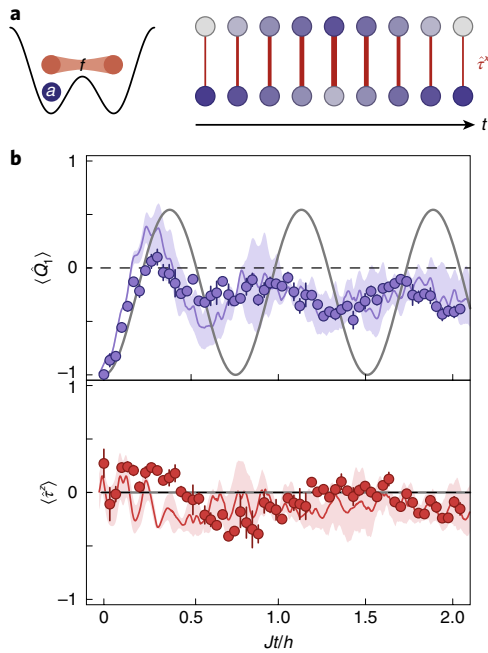
Fig. 3 | Dynamics of the matter–gauge system prepared initially in an eigenstate of the electric field $\hat{\tau}^x$. a, Illustration of the gauge-invariant initial state $|\psi_0^x\rangle = |a,0\rangle \otimes (|f,0\rangle + |0,f\rangle)/\sqrt{2}$ and the expected dynamics according to Hamiltonian (equation (4)). **b**, Measured expectation values of the $\mathbb{Z}_2$ charge $\langle \hat{Q}_1 \rangle$ (blue points) and $\mathbb{Z}_2$ gauge field $\langle \hat{\tau}^z \rangle$ (red points) for $\omega = 2\pi \times 4{,}320$ Hz. Each data point represents the mean of at least three individual experimental results and the error bars denote the standard deviation. The blue and red lines and shadings show a numerical analysis using time-dependent exact diagonalization, which includes averaging of the observables in the presence of an inhomogeneous tilt distribution $\Delta(x,y,z)$ approximated by a normal distribution with standard deviation $\Delta_\sigma/h = 0.44(2)$ kHz, which was independently calibrated (Supplementary Information). The blue and red solid lines are the median and the shading represents the 1σ confidence interval obtained with a bootstrap analysis of 1,000 repetitions. All calculations are performed using the independently calibrated experimental parameters, $J/h = 587(3)$ Hz, $\Delta_f/h = 4.19(3)$ kHz, $U/h = 3.85(7)$ kHz and taking into account additional terms that appear in the extended Bose–Hubbard model (Supplementary Information). The grey solid lines are the ideal dynamics according to equations (4) and (6).
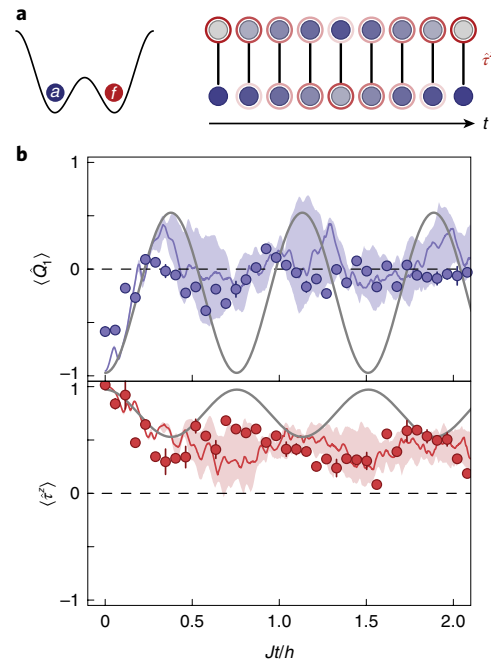
Fig. 4 | Dynamics of the matter–gauge system prepared initially in an eigenstate of the gauge field $\hat{\tau}^z$. a, Schematic of the initial state $|\psi_0^z\rangle = |a,0\rangle \otimes |0,f\rangle$ and the expected dynamics. Brightness of the red circles illustrate the expectation value of $\hat{\tau}^z$. **b**, Measured expectation values of the $\mathbb{Z}_2$ charge $\langle \hat{Q}_1 \rangle$ (blue points) and the $\mathbb{Z}_2$ gauge field $\langle \hat{\tau}^z \rangle$ (red points) for $\omega = 2\pi \times 4{,}314$ Hz. Each data point represents the mean of at least three individual experimental results and the error bars denote the standard deviation. The blue and red lines and shadings show a numerical analysis using time-dependent exact diagonalization, with $J/h = 578(3)$ Hz, $\Delta_f/h = 4.19(3)$ kHz, $U/h = 3.85(7)$ kHz and $\Delta_\sigma/h = 0.46(2)$ kHz as explained in the caption of Fig. 3b and the Supplementary Information. The blue and red solid lines are the median and the shading represents the 1σ confidence interval obtained with a bootstrap analysis of 1,000 repetitions. The grey solid lines are the ideal dynamics according to equations (4) and (6).

state-resolved detection techniques[29]. They provide direct access to the state-resolved density on each site of the double well n_j^a and n_j^f, averaged over the entire 3D array of double-well realizations. The experimental results are shown in Fig. 3b for $U/J = 6.6$ and $\phi = 0$. As expected, we find that the charge oscillates, while the dynamics of the f particle is strongly suppressed. We observe a larger characteristic oscillation frequency for the a particle compared to the prediction of equation (6) (grey line, Fig. 3b). This is predominantly caused by an inhomogeneous tilt distribution $\Delta(x,y,z)$ present in our system. Taking the inhomogeneity into account, the numerical analysis of the full time-dependence according to equation (3) (solid blue line, Fig. 3b) shows good agreement with the experimental results. The fast oscillations both in the data and the numerics are due to the micromotion at non-stroboscopic times.

The f particle is initially prepared in an eigenstate of the electric field operator $\hat{\tau}^x$, which corresponds to an equal superposition of the particle on both sites of the double-well potential, that is, $\langle \hat{\tau}^z(t=0)\rangle = 0$. The $\mathbb{Z}_2$ electric field follows the oscillation of the matter particle in a correlated manner to conserve the local quantities g_j. At the same time the expectation value of the gauge field $\langle \hat{\tau}^z(t)\rangle$

is expected to remain zero at all times. This is a non-trivial result, which is a direct consequence of the $\mathbb{Z}_2$-symmetry constraints. In contrast, a resonantly driven double-well system with $\Delta_f = 0$, which does not exhibit $\mathbb{Z}_2$ symmetry, would show dynamics with equal oscillation amplitudes for the a and f particles. In the experiment we clearly observe suppressed dynamics for the f particle, which is a signature of the experimental realization of the $\mathbb{Z}_2$ symmetry (Fig. 3b). Deviations between the time-dependent numerical analysis and the experimental results are most likely to be due to an imperfect initial state, residual energy offsets and finite ramp times.

In a second set of experiments we study the dynamics where the gauge field particle is initialized in an eigenstate of the gauge field operator $\hat{\tau}^z$, while the matter particle is again localized on site $j = 1$, $|\psi_0^z\rangle = |a,0\rangle \otimes |0,f\rangle$ (Fig. 4a). Here, the system is in a coherent superposition of the two subsectors with $g_1 = -g_2 = \pm 1$ and the expectation value of the locally conserved operators are $\langle \hat{G}_1 \rangle = \langle \hat{G}_2 \rangle = 0$. Note that there is no coupling between different subsectors according to Hamiltonian (equation (4)). The basic dynamics can be understood in the two limiting cases of the model. For $J_f \ll J_a$ the electric field vanishes and the system is dominated by the gauge field $\hat{\tau}^z$. In this limit, a system prepared in an eigenstate of $\hat{\tau}^z$ will remain in this eigenstate because $\hat{\tau}^z$ commutes with Hamiltonian (4) for $J_f = 0$. In the opposite regime ($J_f \gg J_a$), where the electric field dominates, $\langle \hat{\tau}^z \rangle$ oscillates between the two eigenvalues. The dynamics of the $\mathbb{Z}_2$ charge on the other hand is still determined
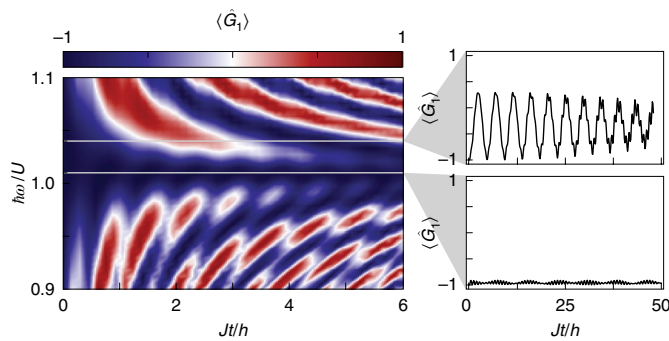
Fig. 5 | Finite-frequency corrections to the effective Floquet Hamiltonian (equation (4)). Stroboscopic dynamics of the expectation value of the local $\mathbb{Z}_2$-symmetry operator $\langle \hat{G}_1 \rangle$ for $|\psi_0^x\rangle$, with $g_1 = -1$, based on Hamiltonian (equation (3)) for different driving frequencies ω. The panels on the right show examples of the time traces for $\hbar\omega \approx 1.04U$ (top) and $\hbar\omega = 1.01U$ (bottom).

by equation (6). In the experiment we probe the intermediate regime at $J_f/J_a \approx 0.54$ for $U/J = 6.7$ and $\phi = \pi$ (Fig. 4b). The dynamics agrees with the ideal evolution (grey line, Fig. 4b) for short times. For longer times it deviates due to the averaging over the inhomogeneous tilt distribution $\Delta(x, y, z)$, which is well captured by the full time dynamics according to Hamiltonian (equation (3)) (red and blue lines, Fig. 4b). Notably, $\langle \hat{\tau}^z \rangle$ exhibits a non-zero average value.

An important requirement for quantum simulations of gauge theories is the exact implementation of the local symmetry constraints to assure that $\langle \hat{G}_j \rangle$ is conserved for all times. Since we do not have direct access to $\langle \hat{G}_j \rangle$ experimentally, we study the implications of symmetry-breaking terms numerically. The dominant contribution stems from the inhomogeneous tilt distribution $\Delta(x, y, z)$, which, however, can be avoided in future experiments by generating homogeneous box potentials. The second type of gauge-variant terms is coupling processes that do not fulfil the constraints of Gauss's law. These are correlated two-particle tunnelling and nearest-neighbour interactions, which are known to exist in interacting lattice models[55]. For our experimental parameters these terms are on the order of $0.03J$ and can be neglected for the timescale of the observed dynamics (Supplementary Information). The same gauge-variant processes appear in the higher-order terms of the Floquet expansion for finite U/J (refs. [44–46]). We study them analytically by calculating the first-order terms of the expansion and comparing them to numerics (Supplementary Information). In Fig. 5 we show the numerically calculated dynamics for the initial state $|\psi_0^x\rangle$ (Fig. 3a) according to the full time-dependent Hamiltonian (equation (3)) for $U/J = 7$, similar to the experimental values (Fig. 5). We find that in this regime the driving frequency is crucial and defines the timescale for which the $\mathbb{Z}_2$ symmetry of the model remains. In particular, there is an optimal value around $\hbar\omega \approx 1.01U$, where the value of $\langle \hat{G}_1 \rangle$ deviates by <10% even for long evolution times.

In summary, we have studied the dynamics of a minimal model for $\mathbb{Z}_2$ LGTs. Our observations are well described by a full time-dependent analysis of the 3D system. Moreover, we find non-trivial dynamics of the matter and gauge field in agreement with predictions from the ideal $\mathbb{Z}_2$ LGT. We further reached a good understanding of relevant symmetry-breaking terms. The dominant processes we identified are species-independent energy offsets between neighbouring sites and correlated two-particle tunnelling terms[55], which can be suppressed in future experiments. We have also provided important insights into the applicability of Floquet schemes. While the Floquet parameters can be fine-tuned in certain cases to ensure gauge invariance, this complication can be avoided by reaching the high-frequency limit[44–46] to minimize

finite-frequency corrections. In experiments this could be achieved using Feshbach resonances to increase the inter-species scattering length. This, however, comes at the cost of enhanced correlated tunnelling processes, which in turn can be suppressed by increasing the lattice depth (Supplementary Information). Numerical studies further indicate that certain experimental observables are robust to gauge-variant imperfections[56,57], which may facilitate future experimental implementations. We anticipate that the double-well model demonstrated in this work will serve as a stepping stone for experimental studies of $\mathbb{Z}_2$ LGTs coupled to matter in extended 1D and 2D systems, which can be realized by coupling many double-well links along a 1D chain (Supplementary Information) or in a ladder configuration[33]. Finally, the use of state-dependent optical lattices could further enable an independent tunability of the matter- and gauge-particle tunnelling terms.

Data availability
The data that support the plots within this paper and other findings of this study are available from the corresponding author on reasonable request.

Code availability
The code that supports the plots within this paper are available from the corresponding author on reasonable request.

Online content
Any methods, additional references, Nature Research reporting summaries, source data, statements of code and data availability and associated accession codes are available at https://doi.org/10.1038/s41567-019-0649-7.

References
1. Wilson, K. G. Confinement of quarks. *Phys. Rev. D* **10**, 2445–2459 (1974).
2. Kogut, J. B. An introduction to lattice gauge theory and spin systems. *Rev. Mod. Phys.* **51**, 659–713 (1979).
3. Wen, X.-G. *Quantum Field Theory of Many-Body Systems* (Oxford University Press, 2004).
4. Levin, M. & Wen, X.-G. Colloquium: photons and electrons as emergent phenomena. *Rev. Mod. Phys.* **77**, 871–879 (2005).
5. Lee, P. A., Nagaosa, N. & Wen, X.-G. Doping a Mott insulator: physics of high temperature superconductivity. *Rev. Mod. Phys.* **78**, 17–85 (2006).
6. Ichinose, I. & Matsui, T. Lattice gauge theory for condensed matter physics: ferromagnetic superconductivity as its example. *Mod. Phys. Lett. B* **28**, 1430012 (2014).
7. Aoki, S. et al. Review of lattice results concerning low-energy particle physics. *Eur. Phys. J. C* **77**, 112 (2017).
8. Troyer, M. & Wiese, U.-J. Computational complexity and fundamental limitations to fermionic quantum Monte Carlo simulations. *Phys. Rev. Lett.* **94**, 170201 (2005).
9. Alford, M. G., Schmitt, A., Rajagopal, K. & Schäfer, T. Color superconductivity in dense quark matter. *Rev. Mod. Phys.* **80**, 1455–1515 (2008).
10. Buyens, B., Verstraete, F. & Acoleyen, K. V. Hamiltonian simulation of the Schwinger model at finite temperature. *Phys. Rev. D* **94**, 085018 (2016).
11. Bañuls, M. C. et al. Towards overcoming the Monte Carlo sign problem with tensor networks. *EPJ Web Conf.* **137**, 04001 (2017).
12. Silvi, P., Rico, E., Dalmonte, M., Tschirsich, F. & Montangero, S. Finite-density phase diagram of a $(1 + 1) − d$ non-abelian lattice gauge theory with tensor networks. *Quantum* **1**, 9 (2017).
13. Gazit, S., Randeria, M. & Vishwanath, A. Emergent Dirac fermions and broken symmetries in confined and deconfined phases of Z_2 gauge theories. *Nat. Phys.* **13**, 484–490 (2017).
14. Weimer, H., Müller, M., Lesanovsky, I., Zoller, P. & Büchler, H. P. A Rydberg quantum simulator. *Nat. Phys.* **6**, 382–388 (2010).
15. Blatt, R. & Roos, C. F. Quantum simulations with trapped ions. *Nat. Phys.* **8**, 277–284 (2012).
16. Gross, C. & Bloch, I. Quantum simulations with ultracold atoms in optical lattices. *Science* **357**, 995–1001 (2017).
17. Romero, G., Solano, E. & Lamata, L. in *Quantum Simulations with Photons and Polaritons* (ed. Angelakis, D.) 153–180 (Springer, 2017).

18. Tagliacozzo, L., Celi, A., Zamora, A. & Lewenstein, M. Optical abelian lattice gauge theories. *Ann. Phys.* **330**, 160–191 (2013).
19. Wiese, U.-J. Ultracold quantum gases and lattice systems: quantum simulation of lattice gauge theories. *Ann. Phys.* **525**, 777–796 (2013).
20. Zohar, E., Cirac, J. I. & Reznik, B. Quantum simulations of lattice gauge theories using ultracold atoms in optical lattices. *Rep. Prog. Phys.* **79**, 014401 (2015).
21. Dalmonte, M. & Montangero, S. Lattice gauge theory simulations in the quantum information era. *Contemp. Phys.* **57**, 388–412 (2016).
22. Notarnicola, S. et al. Discrete Abelian gauge theories for quantum simulations of QED. *J. Phys. A* **48**, 30FT01 (2015).
23. Kasper, V., Hebenstreit, F., Jendrzejewski, F., Oberthaler, M. K. & Berges, J. Implementing quantum electrodynamics with ultracold atomic systems. *New J. Phys.* **19**, 023030 (2017).
24. Kuno, Y., Sakane, S., Kasamatsu, K., Ichinose, I. & Matsui, T. Quantum simulation of (1 + 1)-dimensional U(1) gauge-Higgs model on a lattice by cold Bose gases. *Phys. Rev. D* **95**, 094507 (2017).
25. Zhang, J. et al. Quantum simulation of the universal features of the polyakov loop. *Phys. Rev. Lett.* **121**, 223201 (2018).
26. Aidelsburger, M., Nascimbène, S. & Goldman, N. Artificial gauge fields in materials and engineered systems. *C. R. Phys.* **19**, 394–432 (2018).
27. Clark, L. W. et al. Observation of density-dependent gauge fields in a bose-einstein condensate based on micromotion control in a shaken two-dimensional lattice. *Phys. Rev. Lett.* **121**, 030402 (2018).
28. Anderlini, M. et al. Controlled exchange interaction between pairs of neutral atoms in an optical lattice. *Nature* **448**, 452–456 (2007).
29. Trotzky, S. et al. Time-resolved observation and control of superexchange interactions with ultracold atoms in optical lattices. *Science* **319**, 295–299 (2008).
30. Dai, H.-N. et al. Four-body ring-exchange interactions and anyonic statistics within a minimal toric-code Hamiltonian. *Nat. Phys.* **13**, 1195–1200 (2017).
31. Klco, N. et al. Quantum-classical computation of schwinger model dynamics using quantum computers. *Phys. Rev. A* **98**, 032331 (2018).
32. Martinez, E. A. et al. Real-time dynamics of lattice gauge theories with a few-qubit quantum computer. *Nature* **534**, 516–519 (2016).
33. Barbiero, L. et al. Coupling ultracold matter to dynamical gauge fields in optical lattices: from flux-attachment to Z_2 lattice gauge theories. Preprint at https://arxiv.org/abs/1810.02777 (2018).
34. Zohar, E., Farace, A., Reznik, B. & Cirac, J. I. Digital quantum simulation of Z_2 lattice gauge theories with dynamical fermionic matter. *Phys. Rev. Lett.* **118**, 070501 (2017).
35. Horn, D., Weinstein, M. & Yankielowicz, S. Hamiltonian approach to $Z(N)$ lattice gauge theories. *Phys. Rev. D* **19**, 3715–3731 (1979).
36. Ju, H. & Balents, L. Finite-size effects in the Z_2 spin liquid on the kagome lattice. *Phys. Rev. B* **87**, 195109 (2013).
37. González-Cuadra, D., Dauphin, A., Grzybowski, P. R., Lewenstein, M. & Bermudez, A. Symmetry-breaking topological insulator in the Z_2 Bose-Hubbar dmodel. *Phys. Rev. B* **99**, 045139 (2019).
38. Kitaev, A. Y. Fault-tolerant quantum computation by anyons. *Ann. Phys.* **303**, 2–30 (2003).
39. Keilmann, T., Lanzmich, S., McCulloch, I. & Roncaglia, M. Statistically induced phase transitions and anyons in 1d optical lattices. *Nat. Commun.* **2**, 361 (2011).
40. Greschner, S. & Santos, L. Anyon hubbard model in one-dimensional optical lattices. *Phys. Rev. Lett.* **115**, 053002 (2015).
41. Bermudez, A. & Porras, D. Interaction-dependent photon-assisted tunneling in optical lattices: a quantum simulator of strongly correlated electrons and dynamical gauge fields. *New. J. Phys.* **17**, 103021 (2015).
42. Sträter, C., Srivastava, S. C. L. & Eckardt, A. Floquet realization and signatures of one-dimensional anyons in an optical lattice. *Phys. Rev. Lett.* **117**, 205303 (2016).
43. Goldman, N., Dalibard, J., Aidelsburger, M. & Cooper, N. R. Periodically driven quantum matter: the case of resonant modulations. *Phys. Rev. A* **91**, 033632 (2015).
44. Goldman, N. & Dalibard, J. Periodically driven quantum systems: effective hamiltonians and engineered gauge fields. *Phys. Rev. X* **4**, 031027 (2014).
45. Bukov, M., D'Alessio, L. & Polkovnikov, A. Universal high-frequency behavior of periodically driven systems: from dynamical stabilization to Floquet engineering. *Adv. Phys.* **64**, 139–226 (2015).
46. Eckardt, A. Colloquium: atomic quantum gases in periodically driven optical lattices. *Rev. Mod. Phys.* **89**, 011004 (2017).
47. Ma, R. et al. Photon-assisted tunneling in a biased strongly correlated bose gas. *Phys. Rev. Lett.* **107**, 095301 (2011).
48. Chen, Y.-A. et al. Controlling correlated tunneling and superexchange interactions with ac-driven optical lattices. *Phys. Rev. Lett.* **107**, 210405 (2011).
49. Meinert, F., Mark, M. J., Lauber, K., Daley, A. J. & Nägerl, H.-C. Floquet engineering of correlated tunneling in the bose-hubbard model with ultracold atoms. *Phys. Rev. Lett.* **116**, 205301 (2016).
50. Görg, F. et al. Realization of density-dependent Peierls phases to engineer quantized gauge fields coupled to ultracold matter. *Nat. Phys.* https://doi.org/10.1038/s41567-019-0615-4 (2019).
51. Keay, B. J. et al. Dynamic localization, absolute negative conductance, and stimulated, multiphoton emission in sequential resonant tunneling semiconductor superlattices. *Phys. Rev. Lett.* **75**, 4102–4105 (1995).
52. Lignier, H. et al. Dynamical control of matter-wave tunneling in periodic potentials. *Phys. Rev. Lett.* **99**, 220403 (2007).
53. Sias, C. et al. Observation of photon-assisted tunneling in optical lattices. *Phys. Rev. Lett.* **100**, 63 (2008).
54. Mukherjee, S. et al. Modulation-assisted tunneling in laser-fabricated photonic Wannier–Stark ladders. *New J. Phys.* **17**, 115002 (2015).
55. Scarola, V. W. & Sarma, S. D. Quantum phases of the extended bose-hubbard hamiltonian: possibility of a supersolid state of cold atoms in optical lattices. *Phys. Rev. Lett.* **95**, 033003 (2005).
56. Banerjee, D. et al. Atomic quantum simulation of U(N) and SU(N) non-Abelian lattice gauge theories. *Phys. Rev. Lett.* **110**, 125303 (2013).
57. Kühn, S., Cirac, J. I. & Bañuls, M.-C. Quantum simulation of the Schwinger model: a study of feasibility. *Phys. Rev. A* **90**, 042305 (2014).

Acknowledgements

Author contributions

C.S., F.G., N.G. and M.A. planned the experiment and performed theoretical calculations. C.S. and M.B. performed the experiment and analysed the data with M.A. All authors discussed the results and contributed to the writing of the paper.

Competing interests

The authors declare no competing interests.

Additional information

Publisher's note: Springer Nature remains neutral with regard to jurisdictional claims in published maps and institutional affiliations.